Cyanide-bridged coordination polymers constructed from lanthanide ions and octacyanometallate building-blocks

Gao, Y.; Viciano-Chumillas, M.; Toader, A.M.; Teat, Simon J.; Ferbinteanu, M.; Tanase, S.

RESEARCH ARTICLE

Cyanide-bridged coordination polymers constructed from lanthanide ions and octacyanometallate building-blocks†

Yuan Gao,[a] Marta Viciano-Chumillas, [b] Ana Maria Toader,[c] Simon J. Teat, [d]
Marilena Ferbinteanu [*e] and Stefania Tanase [*a]

A new series of cyanide-bridged assemblies, {KH[Ln$_2$(2,3-pzdc)$_2$(CH$_3$OH)(H$_2$O)$_7$][M(CN)$_8$]}·5H$_2$O (Ln^{3+} = Nd, Gd, Tb, and Dy; M^{4+} = Mo and W), were synthesised by self-assembling lanthanide ions and octacyano-metallate ions in the presence of pyrazine-2,3-dicarboxylic acid (2,3-H$_2$pzdc). These compounds have a 3D structure in which octagon-like Ln$_4$M$_4$(CN)$_8$ rings are connected through a second Ln^{3+} center *via* the carboxylate groups of one 2,3-pzdc. The resulting 1D channels are filled with K$^+$ ions and lattice water molecules. The temperature and field dependent magnetization studies as well as *ab initio* calculations indicate weak ferromagnetic interactions between the Gd^{3+} ions within the GdMo compound whilst no magnetic interactions exist in GdW analogues. The magnetic properties of Nd^{3+}, Tb^{3+} and Dy^{3+} compounds are strongly dominated by the magnetic anisotropy of the lanthanide ions, irrespective of the octacyanometallate building-block used.

Introduction

Research on molecular magnetic materials stems from the interest in understanding the magnetic exchange interactions, performing magneto-structural correlations,[1–4] and curiosity in exotic magnetic phenomena (*e.g.* single molecular magnets,[5–7] single chain magnets[8–11]) as well as their potential applications in high-tech fields, including magnetic refrigeration,[13,14] quantum computing[15] and information storage.[16] Lanthanide ions, with high spin, large intrinsic magnetic anisotropy and quantum tunneling of the magnetization (QTM), are the natural choices for molecular magnetic materials.[17,18] Specifically, the magnetic anisotropy is the key property to achieve permanent and switchable magnetization.[12] However, lanthanide ions have inner shell magnetic orbitals, as well as

large coordination spheres and flexible coordination geometries. Therefore, achieving strong magnetic exchange and inserting lanthanide ions into highly ordered structures are difficult tasks.[19–26] One approach to overcome these challenges is by linking the lanthanide ions to other paramagnetic ions through small bridging ligands and using building-blocks that allow controlling the final structural topology.[27–29] Thus, combining lanthanide ions and polycyanometallate building-blocks exploits not only the bridging coordination of the cyanide ligand but also its ability to provide an exchange path that mediates the interaction between the electrons localized on paramagnetic centers. This approach afforded a great diversity of structural architectures displaying a broad range of magnetic phenomena.[30–32] Moreover, the cyanide-bridged molecular assemblies containing lanthanide ions are gaining increased interest also due to their multifunctional properties. These are based on the combination of multiple physical properties, including optical and magnetic properties,[33] optical and electrical properties,[34] and gas separation properties.[27]

Most of the lanthanide-based cyanide-bridged systems have 1D or 2D network structures and only a few 3D assemblies are reported.[30,33–35] We showed previously that assembling lanthanide ions and octacyanometallate building-blocks in the presence of 5-methyl-2-pyrazine carboxylic acid (Hmpca) as the ligand is an efficient route to build isostructural three-dimensional networks.[32] Therefore, we extended this strategy to other pyrazine-carboxylate linkers, by replacing the mono-carboxylate ligand Hmpca with another small linker, namely

aVan't Hoff Institute for Molecular Sciences, University of Amsterdam, Science Park 904, 1098 XH Amsterdam, Netherlands. E-mail: s.grecea@uva

bInstituto de Ciencia Molecular (ICMol), Universidad de Valencia, c/Catedrático José Beltrán, 2, 46980 Paterna, Spain

cInstitute of Physical Chemistry, Splaiul Independentei 202, Bucharest 060021, Romania

dAdvanced Light Source, Lawrence Berkeley National Laboratory, Berkeley, USA

eFaculty of Chemistry, Inorganic Chemistry Department, University of Bucharest, Dumbrava Rosie 23, Bucharest 020462, Romania. E-mail: marilena.cimpoesu@g.unibuc.ro

This journal is © the Partner Organisations 2018

Inorg. Chem. Front., 2018, **5**, 1967–1977 | **1967**

pyrazine-2,3-dicarboxylic acid (2,3-H$_2$pzdc). This approach aimed at studying the influence of the organic linker on the final 3D structural topology. The 2,3-H$_2$pzdc ligand has a C_2 symmetry and it is commonly used to build extended systems. Its coordination to d-block transition metal ions is studied in detail and several lanthanide-based 3D coordination networks were also synthesised.[36–38] In this study we discuss the crystal structure of a new series of isostructural compounds, {KH[Ln$_2$(2,3-pzdc)$_2$(CH$_3$OH)(H$_2$O)$_7$][M(CN)$_8$]}·5H$_2$O (Ln^{3+} = Nd, Gd, Tb, and Dy; M^{4+} = Mo and W) and their corresponding magnetic properties, with a focus on understanding the magnetic anisotropy of the lanthanide ions.

Results and discussion

Synthesis and structural characterization

A series of isostructural cyanide-bridged coordination polymers, {KH[Ln$_2$(2,3-pzdc)$_2$(CH$_3$OH)(H$_2$O)$_7$][M(CN)$_8$]}·5H$_2$O (Ln^{3+} = Nd, Gd, Tb, and Dy; M^{4+} = Mo and W; NdMo **1**, GdMo **2**, TbMo **3**, DyMo **4**, NdW **5**, GdW **6**, TbW **7**, and DyW **8**) were synthesized by self-assembling lanthanide ions (Ln^{3+}) and the octacyanometallate building-blocks [M(CN)$_8$]$^{4-}$ in an aqueous solution and in the presence of pyrazine-2,3-dicarboxylic acid (2,3-H$_2$pzdc) as the bifunctional (chelate and bridging) ligand. Attempts to grow single-crystals have shown that the polarity of the solvent used for crystallization plays a key role, with methanol giving the materials with the highest purity and yield. The purity of the compounds was confirmed by elemental analysis, FTIR, PXRD and TGA-DSC studies (Fig. S1–S3†).

The FTIR spectra of all compounds show the $\nu_{C\equiv N}$ stretching vibrations in the range of 2090–2120 cm^{-1}, indicating the presence of both terminal and bridging cyanide groups. Furthermore, the ν_{COO^-} stretching vibrations around 1620 and 1570 cm^{-1} are shifted towards lower energies as compared with the free ligand (1754 and 1713 cm^{-1}),[39] thus confirming the coordination of carboxylate groups to the lanthanide ions. The simulated PXRD patterns of **1**–**8** are consistent with the simulated PXRD pattern using the single-crystal data of **5**. This indicates that the above synthesis method can be applied for various lanthanide ions (Nd^{3+}, Gd^{3+}, Tb^{3+}, and Dy^{3+}) and [M(CN)$_8$]$^{4-}$ (M = Mo and W) building-blocks. The multiple XRD peaks suggest the low symmetry of this series of compounds, in agreement with the single-crystal XRD parameters (group space $C2/c$). The water content was confirmed by thermogravimetric (TGA) and elemental analysis. The 6.3% (calc. 6.9%) weight loss below 100 °C corresponds to the removal of the lattice water. The second weight loss of *ca.* 5.3% (calc. 5.6%) below 180 °C belongs to the coordinated water molecules. The endothermic DSC effects associated with these weight losses suggest that no major structural changes occur within the framework upon water removal. The framework collapses around 400 °C.

Crystal data refinement was possible only for compound **5**, and therefore only the structure of this compound will be discussed in detail. Compound **5** crystallizes in the monoclinic
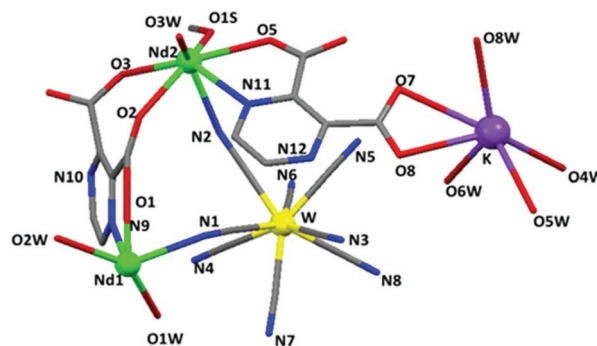
Fig. 1 The asymmetric unit of **5**. The hydrogen atoms and the lattice water molecules are omitted for clarity.

space group $C2/c$. The asymmetric unit of **5** (Fig. 1) consists of two Nd^{3+} ions, two deprotonated 2,3-pyrazinedicarboxylate ligands, one [W(CN)$_8$]$^{4-}$ unit and one K$^+$ ion. Fig. 2 (top) shows that both Nd^{3+} ions are nine-coordinated, displaying a trigonal-prismatic geometry, but they have different coordination surroundings. The Nd1 is surrounded by two carboxylate oxygen atoms (O1 and O8), three nitrogen atoms (N1, N3, and N8) from three cyanide groups and two nitrogen atoms (N9 and N12) from different pzdc^{2-} rings. The remaining two coordination sites are occupied by two water molecules. The
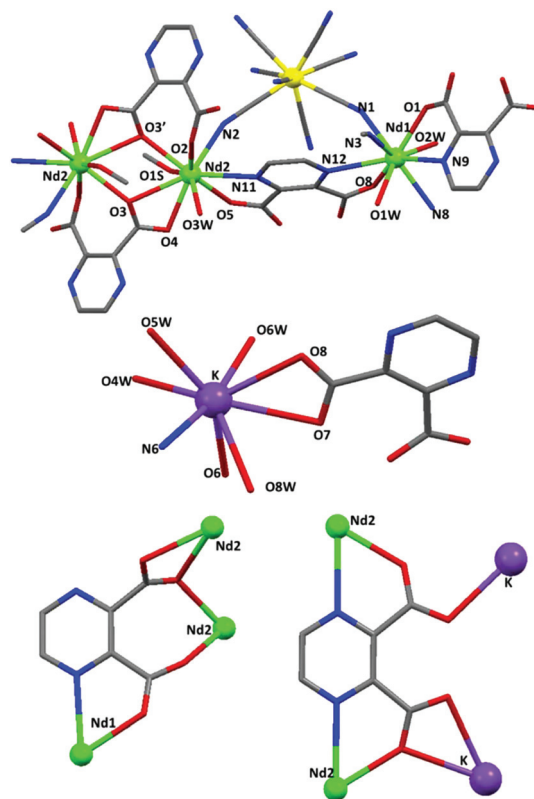
Fig. 2 The coordination environments of the Nd^{3+} (top) and K$^+$ ions (middle) and the coordination modes of the pzdc^{2-} ligands (bottom) in **5**.

1968 | *Inorg. Chem. Front.*, 2018, **5**, 1967–1977

This journal is © the Partner Organisations 2018

Nd2 center is coordinated by five oxygen atoms (O2, O3, O3′, O4, and O5) coming from the carboxylate groups of the three pzdc^{2-} ligands and one nitrogen atom (N11) from one pzdc^{2-} ligand. The heptadentate ligand provides the *N,O*-bidentate chelating mode whilst the hexadentate ligand binds only through one oxygen from one carboxylate group. The coordination of a water molecule, a bridging cyanide ligand and a methanol molecule completes the coordination number of nine of the Nd2. The Nd–O and Nd–N bond lengths range from 2.430 to 2.716 Å. Each K$^+$ ion is connected to three oxygen atoms from the two pzdc^{2-} ligands and one nitrogen (N6) from [W(CN)$_8$]$^{4-}$ and the remaining four coordination sites are occupied by four H$_2$O molecules. Thus, the [W(CN)$_8$]$^{4-}$ unit contains three bridging cyanide ligands coordinated to two Nd^{3+} ions and one K$^+$ ion. The average K–O$_{pzdc}$ bond distance (2.900 Å) is similar to the average K–O$_w$ bond distance (2.940 Å), as a result of a very dense molecular structure. Generally, K$^+$ is a key cation in stabilizing the crystal packing due to its low polarizability and high affinity for oxygen donor molecules.[40]

Fig. 2 (bottom) shows the coordination of the two pzdc^{2-} ligands to the Nd^{3+} and K$^+$ ions. One ligand binds to three Nd^{3+} ions, namely one Nd1 and two Nd2. The second ligand is coordinated to two Nd2 and two K$^+$ ions. The Nd1 centers and the [W(CN)$_8$]$^{4-}$ building-blocks are linked in an alternating fashion and form a 2D network containing the octagon-like rings (Nd1)$_4$W$_4$(CN)$_8$ (Fig. 3, top). Neighbouring 2D networks are linked to each other *via* Nd2 ions giving a 3D structure with open channels (Fig. 3, bottom). Notably, this structural topology is similar to the 3D topology obtained using the

mpca$^-$ ligand.[32] In the present case, the dianionic 2,5-pzdc ligand favours the formation of Nd$_3$-type clusters as secondary building units and the K$^+$ ions compensate for the negative charge of the 3D framework and sit in the octagon-like 1D chains. Within the Nd$_3$ cluster, the shortest Nd···Nd intramolecular distances are: 6.630 Å for Nd1···Nd2 and 4.347 Å for Nd2···Nd2, respectively. The shortest Nd1···W distance is 5.261 Å whilst the shortest Nd1···Nd1 distance is 10.622 Å. The overall 3D molecular structure is further stabilized by multiple hydrogen-bonding interactions established between the carboxylate groups of the organic linkers, the water and methanol molecules as well, as the cyanide terminal groups. This might also explain the higher thermal stability of the studied compounds as compared with the thermal stability of their analogues obtained from the mpca$^-$ ligand.[27]

Magnetic properties

The presence of the Nd1(Nd2)$_2$ type of clusters bridged by diamagnetic octacyanometallate building-blocks (see Fig. 2, top) in the 3D molecular structure of the compounds studied as well as the short Nd···Nd distances (4.347–6.630 Å) make these isostructural materials interesting for studying their magnetic properties. Therefore, the temperature-dependent magnetic susceptibility data of the compacted polycrystalline samples of **1–8** were measured in the 1.8–300 K temperature domain, in a 0.1 T magnetic field (Fig. 4). The experimental data are complemented with computed simulations which will be detailed in the following section. The $\chi_M T$ values at room temperature are 3.14 (**1**), 16.46 (**2**), 24.32 (**3**), 29.12 (**4**), 3.19 (**5**), 15.69 (**6**), 23.70 (**7**) and 28.73 cm^3 K mol^{-1} (**8**). These values are close to those expected for two lanthanide(III) ions: $\chi_M T_{Nd2}$ = 3.28 cm^3 K mol^{-1} with S = 3/2, L = 6, ^{4}I$_{9/2}$, g = 8/11; $\chi_M T_{Gd2}$ = 15.74 cm^3 K mol^{-1} with S = 7/2, L = 0, ^{8}S$_{7/2}$, g = 2; $\chi_M T_{Tb2}$ = 23.64 cm^3 K mol^{-1} with S = 3, L = 3, ^{7}F$_6$, g = 3/2 and $\chi_M T_{Dy2}$ = 28.34 cm^3 K mol^{-1} with S = 5/2, L = 5, ^{6}H$_{15/2}$, g = 4/3.[41] With the exception of Gd^{3+} that has a f^7 electronic configuration and an orbital nondegenerate ground state, all the lanthanide ions have orbital degenerate ground states, which are split by spin–orbit (SO) coupling and ligand field (LF) effects.[42–44] The field dependence magnetization curves for compounds **1–8** are shown in Fig. S4.† The magnetization values at 5 T reaches the expected saturation value of 14$N\beta$ (2 Gd^{3+}) for **2** and **6**, whilst for the other compounds, the magnetization values do not reach the saturation values for two isolated Ln^{3+} ions [M = 6.54$N\beta$ (2 Nd^{3+}), 18$N\beta$ (2Tb^{3+}) and 20$N\beta$ (2 Dy^{3+})]. This fact is mainly due to the crystal field effects on the Ln^{3+} ions.

The $\chi_M T$ product of the Tb^{3+} (**3** and **7**) and Dy^{3+} (**4** and **8**) compounds decreases smoothly until 25 K and then more pronounced until 2 K. For Nd^{3+} polymers (**1** and **5**), the $\chi_M T$ value decreases constantly from 300 K till 2 K. These behaviors can be ascribed to the spin–orbit coupling and the crystal field effects of the lanthanide ions. By lowering the temperature, the $\chi_M T$ values of **2** and **6** remained constant up to *ca.* 10 K, then increase slightly up to *ca.* 2 K. This behavior suggests the occurrence of very weak ferromagnetic interactions between Gd^{3+} perhaps combined with the ZFS of Gd^{3+} at very low temp-

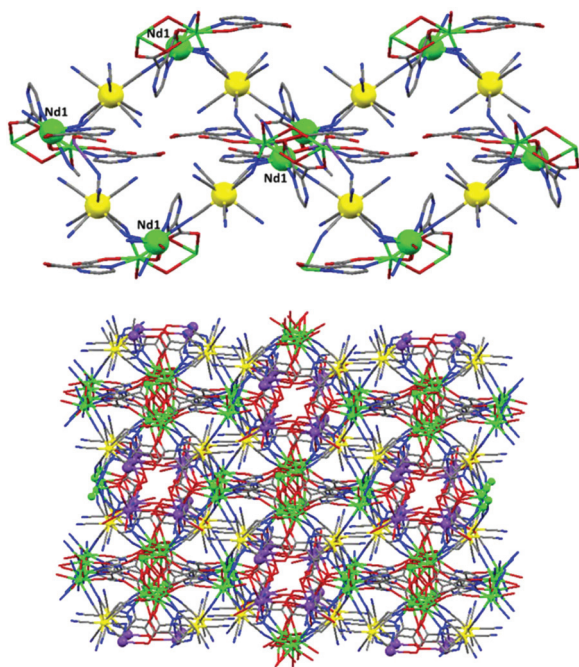
Fig. 3 The 2D connections of Nd1 and [W(CN)$_8$]$^{4-}$ in the molecular structure of **5** (top) and its dense 3D structure (bottom).
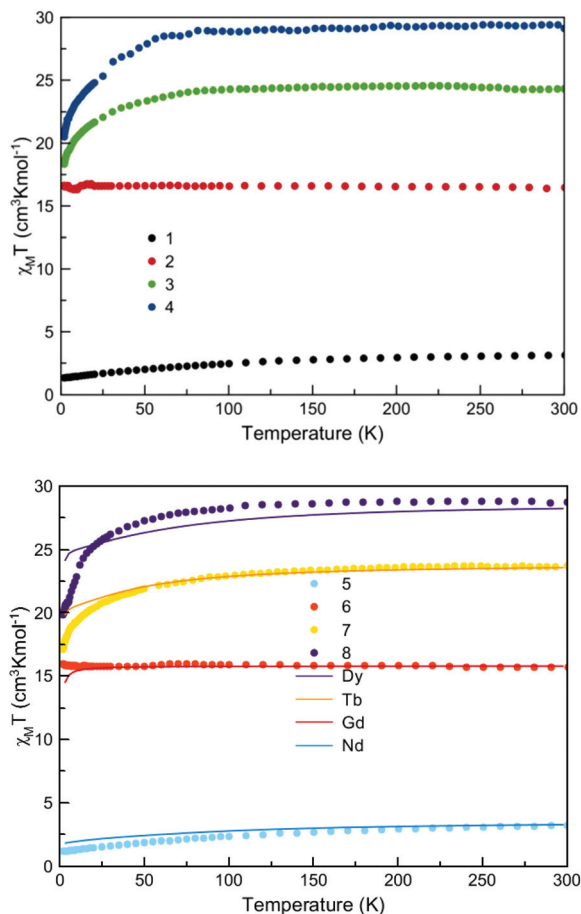
This journal is © the Partner Organisations 2018

Inorg. Chem. Front., 2018, **5**, 1967–1977 | **1969**

Fig. 4 Temperature dependence of $\chi_M T$ of {KH[Ln$_2$(2,3-pzdc)$_2$(CH$_3$OH)(H$_2$O)$_7$][Mo(CN)$_8$]}·5H$_2$O, **1–4** (top) and {KH[Ln$_2$(2,3-pzdc)$_2$(CH$_3$OH)(H$_2$O)$_7$][W(CN)$_8$]}·5H$_2$O, **5–8** (bottom). The continuous lines in the bottom panel mark the *ab initio* simulated curves (*vide infra*).

erature. To get further insight into the nature of the magnetic exchange interactions between the Gd^{3+} ions, we have compared the experimental data to the Brillouin function calculated assuming non-interacting spins, with $S_{Gd} = 7/2$ and $g_{Gd} = 2$. As seen in Fig. S5,† small deviations appear for **2** which can be attributed to the ferromagnetic behaviour whilst the non-interacting limit describes the data for compound **6** quite well. This difference might be explained in terms of different residual contribution from the d-type ion. Namely, the spin orbit coupling silences the magnetism of the d^2 configuration. The parallel pairing of electrons in non-relativistic orbitals turns to a paired configuration in relativistic ones. Because the spin orbit interaction is larger in W than in Mo, the spin-paired configuration is spaced by a larger gap from states with magnetic moment. Therefore, the magnetic response of compound **2** may be larger as compared to **6**, due to such factors.

Although the Ln^{3+}···Ln^{3+} separation is not so large (4.347–6.63 Å), the magnetic interactions between Ln^{3+} ions are usually very weak. Therefore, we also studied the dynamic magnetic properties of all compounds. In a zero dc magnetic field, AC magnetic measurements show no χ''_M signals for all

compounds. However, in the presence of a magnetic field (0.1 and 0.25 T), there is a frequency dependence of the χ''_M values for all compounds, except for **3** and **7**. The fact that the Tb^{3+} compounds do not present a slow relaxation of the magnetization has also been observed in other lanthanide molecular systems.[45] In this work only compound **4** was studied in detail (Fig. S6†). The χ''_M displays a maximum value around 2.70 K which is slightly shifted at higher frequencies and in a 0.1 T applied field; this maximum disappears at low frequencies. Due to the lack of maxima, combined with the fact that there is no clear frequency dependence of the χ''_M, the pre-exponential factor (τ_0) and the effective energy barrier (E_a) were calculated approximately from the linear graphics of $\ln(\chi''_M/\chi_M')$ *versus* $1/T$, assuming only one slow relaxation of the magnetization process (Fig. S7†). Such a methodology was employed successfully in other SMMs.[46,47] The obtained values are $\tau_0 = 6.12 \times 10^{-8}$ s and $E_a = 12.77$ K. Although similar values were determined for other lanthanide compounds,[45] we believe that these values should be considered as a simplification of the system, since there are two different lanthanide centers weakly coupled through a doubly oxide bridge.

Multi-configuration *ab initio* calculations: the d–f exchange coupling and ligand field effects

In order to understand the magnetic properties of the compounds studied, we performed multi-configurational calculations on molecular fragments representing the two distinct crystallographic sites, corresponding to Nd1 and Nd2 in the resolved structure of compound **5**. For each crystallographic species, the symmetric dimer sequences were selected, replacing one lanthanide site by the diamagnetic Lu^{3+} ion. The dimeric fragments are needed for the realistic account of the effects exerted by the bridging ligands, while the artificial replacement of one site by the magnetically silent f^{14} configuration is the appropriate numeric experiment aiming at describing the ligand field around a given ion. A lanthanide with a f^n configuration is accounted for by a CASSCF(n,7), *i.e.* with n electrons in the seven f-type orbitals representing the given problem.

We showed previously[31] that setting *ab initio* calculations for lanthanide complexes is a non-trivial task, the delicate situation being a reliable orbital guess, to initiate the calculations. Therefore, a customized choice is a starting set which is produced by merging the fragment orbitals obtained in preamble for the free lanthanide ion and the remainder of the molecule. This setting describes most appropriately the weakly interacting f shell of the lanthanide ions. The self-consistent canonical molecular orbitals (MOs) are obtained as almost pure f-type atomic orbitals (AOs). Cyanide-bridged lanthanide extended systems are often isostructural series with very similar geometry parameters.[48] Therefore, we have performed the modelling using the same structure for the above discussed series, including Nd^{3+}, Gd^{3+}, Tb^{3+} and Dy^{3+}, respectively. Since we aim for a semi-quantitative description, the small change due to the lanthanide contraction effect, usually confined within 4% variation and taking into account the La^{3+} and Lu^{3+} ions as

1970 | *Inorg. Chem. Front.*, 2018, **5**, 1967–1977

This journal is © the Partner Organisations 2018

extremes, does not affect the range and the ordering of the computed quantities. The assumed unique structure has the advantage of unitary description of the magnetic anisotropy of different ions, driven by the geometry of the local environment. Additionally, CASSCF calculations were performed to account for the LF effects. The resulting set of states correspond to the split of the ground multiplet of each lanthanide ion under the effect of the local environment. Adding the spin–orbit (SO) contribution, one obtains the full description of the magnetic properties at first principles level. The combined CASSCF-SO procedures can be regarded as describing the Ligand Field (LF) split of the J multiplets resulting from a given $^{2S+1}[L]$ spectral term.

Table 1 summarizes the results for Nd^{3+}, Tb^{3+} and Dy^{3+} ions in the model molecules corresponding to sites 1 and 2. Thus, the Nd^{3+} ion has a $J = 9/2$ SO multiplet (resulted from the ^4I parent), which is split in a series of degenerate doublets. The Tb^{3+} ion corresponds to a $J = 6$ quantum number (springing from the ^7F term). Because of the odd $2J + 1$ count, the system does not have doublets, but certain sequences of the spectra can be considered as almost degenerate couples. The Dy^{3+} ion has a $J = 15/2$ quantum number (from ^6H term), the splitting being organized again in a series of doublets. One observes that the total gaps within the multiplets are in the order of several hundreds of reciprocal centimetres, i.e. the expected range of the LF effects of the f shell, thus confirming that the calculation accounted for the effects in a well-tempered balance. One observes that, for each lanthanide ion, the total split is larger in site 1 than in site 2. This is due to the presence of more nitrogen-based strong field ligands in the coordination sphere of site 2. Namely, site 1 has one pyrazine and one cyanide coordination bonds whilst site 2 is surrounded by two pyrazine and three cyanide links.

A detailed characterization of the magnetic anisotropy is achieved by analysing the polar maps of the state-specific mag-

netization function of θ and the φ angular coordinates which corresponds to a given direction inside the coordination sphere, taking the derivative with respect to the field along this axis:

$$M_i(\theta, \varphi) = -\left(\frac{dE_i}{dB}\right)_{\theta,\varphi}.$$

The polar map represents the points at the $\{\theta, \varphi, \text{and } M_i\}$ sets of coordinates, i.e. it consists of a surface with the points in the $\{\theta, \varphi\}$ direction placed at the M_i distance from the selected paramagnetic centre. Usually, the magnetization polar maps have a bi-lobate aspect, the direction of the lobes indicating the easy-magnetization axis, while their size corresponds to the nominal magnetic moment of the given state.

A non-trivial result is the identification of the magnetization axis and the carried effective magnetic moment for each state of the computed magnetic spectrum. Fig. 5 illustrates the ground states of the Nd^{3+}, Tb^{3+} and Dy^{3+} ions in the case of site 1, whilst Fig. 6 corresponds to the site 2. The anisotropic magnetization plots for all the states of the above-mentioned J multiplets of the chosen lanthanide ions and sites are outlined in Fig. S8–S13.† The molecular skeleton is represented at arbitrary scale, the 3D axis frame being based on Bohr magneton units. The orientation of the frame is chosen with the easy axis of the ground state aligned to the z line.

Although J and J_z are not good quantum numbers under a ligand field with low symmetry, a part of the electronic states can still be associated with the J_z projections. In certain cases, the size of the lobes can be estimated as the $|g_J \cdot J_z|$ values, taking the ideal Landé factors of the parent J quantum

Table 1 The CASSCF-SO computed lowest levels corresponding to the LF split of the J ground multiplets of the considered ions and sites. All the values are in cm^{-1}

	Site 1			Site 2		
	Nd	Tb	Dy	Nd	Tb	Dy
1	0.0	0.0	0.0	0.0	0.0	0.0
2	0.0	0.0	0.0	0.0	0.0	0.0
3	100.1	126.7	195.4	42.6	103.5	128.2
4	100.1	127.0	195.4	42.6	104.4	128.2
5	163.3	251.6	342.7	162.2	191.2	229.1
6	163.3	252.4	342.7	162.2	197.0	229.1
7	271.8	365.9	448.5	209.0	247.8	291.8
8	271.8	378.2	448.5	209.0	280.1	291.8
9	332.0	458.7	519.1	293.7	287.7	331.2
10	332.0	504.2	519.1	293.7	351.9	331.2
11		549.2	573.2		356.5	377.1
12		571.5	573.2		447.3	377.1
13		588.1	616.5		448.4	417.4
14			616.5			417.4
15			631.9			491.1
16			631.9			491.1

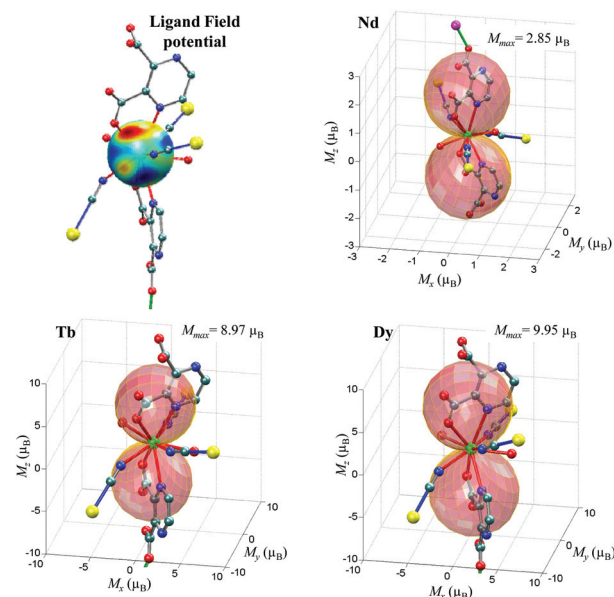**Fig. 5** The computational characterization of site 1: the map of ligand field potential, common for all the lanthanide ions and the easy magnetization axis specific for the ground state of each ion in the modelled environment. Note that the Nd^{3+} vs. Tb^{3+} and Dy^{3+} cases are represented on different scales.

This journal is © the Partner Organisations 2018

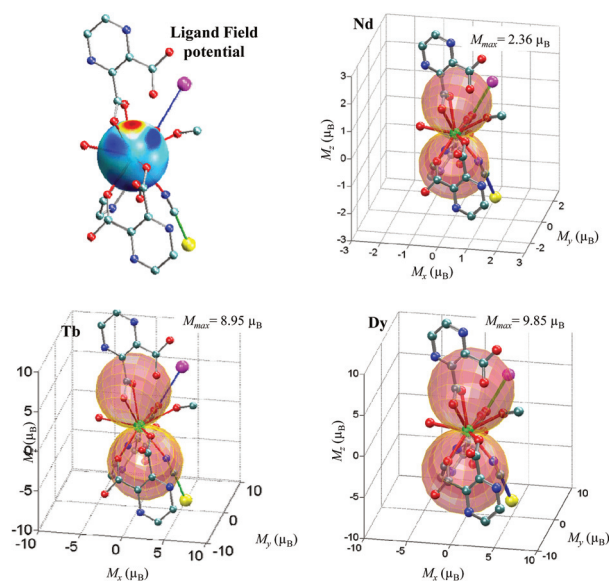Inorg. Chem. Front., 2018, **5**, 1967–1977 | **1971**

Fig. 6 The computational characterization of site 2. The description is similar to that in Fig. 5.

numbers. Such a regularity is retrieved for the ground levels of Tb^{3+} and Dy^{3+} units. For both coordination environments, the extensions of the ground state magnetization lobes are close to the expected values of $9\mu_B$ and $10\mu_B$, respectively. These values are related to the maximal $J_z = \pm6$ and $J_z = \pm15/2$, considering the ideal $g_J = 3/2$ and $g_J = 4/3$, respectively (see the values ascribed on panels from Fig. 5 and 6). For Nd^{3+}, the maximal ideal value is $3.27\mu_B$. The magnetic moment estimated from $g_J = 8/11$ and $J_z = \pm9/2$ is not reached in any state. The actual maximum attained by the ground level is $2.85\mu_B$ for site 1 and $2.36\mu_B$ for site 2.

For the ground state, all the lanthanide ions in a given site type show almost the same easy axis. This can be roughly related to the line undergoing the strongest ligand field, but in the present case the field cannot be assumed as being dominantly axial. In a symmetry which demands an axial pattern, *i.e.* D_{4d} case, the easy magnetization axes of all the states will be on the four-fold axis, the polar maps having lobes with the $|g_J \cdot J_z|$ size. In such a case, the strength of the ligand field will determine only the energy ordering of the states described by the J_z quantum numbers (a generally non-monotonous dependence). The analysis of the full spectrum of state-specific magnetic anisotropy shows a complicated pattern. For instance, for the Nd^{3+} ion from site 1, the magnetization maps of first (ground) and third doublets are aligned on the z axis, while for the second and the fourth doublets, the magnetization maps are intermediates between the axial (bi-lobal) and the in-plane (torus shape) patterns. In the Nd2 site the magnetization lobes of first and second doublets are aligned on the z axis, the third one, approximately on x, while the fourth one goes roughly along the y direction. For Tb^{3+} ions, many states have small intrinsic magnetic moments. Thus, for site 1, the first three couples carry most of the magnetism, and the middle

and the upper parts show maps with small lobes. For site 2, only the first, the second and the last couples, carry a sizeable magnetism. All levels from the fifth to eleventh show weak responses to the magnetic field. The Dy^{3+} has a rich array of polarization maps. For both sites, the first two doublets have the anisotropy along the z axis, the penultimate and last pairs being almost on x and y, respectively, while the middle of the spectrum shows maps with lobes between the chosen Cartesian axes.

In a given series, as a function of the local environment, all the lanthanide congeners have the same ligand field parameters because of the imposed unique geometry. The different magnetic features of the individual ions are related to the specific interplay of the orbital part with the spin components. The ligand field parameters are displayed in the ESI (Tables S1 and S2†) including the suggestive representation of the potential as a color map on the sphere. The ligand field potential can be thought as a sum of a series of parameters (up to 27, for a f site with no symmetry) factoring certain trigonometric-alike expressions (resulted from spherical harmonics), being therefore a function of polar coordinates. Rendering this potential on a sphere, one achieves a clear view of the given set of LF parameters. The areas colored in the yellow to red represent the relatively large ligand field zones (positive values), the green lands average effects, while the blue corresponds to the negative counterpart, usually found in the voids between the ligands. Such maps are given in the left-upper corners of Fig. 5 and 6, different other views being given in Fig. S14 and S15 (see ESI† for details).

It is worth noting a less known technical aspect: the LF potential is affected by the so-called holohedrization effect,[49] because it consists of only components with even behaviour at inversion. This means that the perturbation exerted by a ligand from a direction described by certain x, y and z components is mirrored also on the $-x$, $-y$ and $-z$ antipodes, on a sphere. Then, the positive areas recorded in the ligand field color map are placed not only under the ligands, but also in zones coming, by inversion, in *trans* to a given donor. The stronger fields are occurring on the axis spanning exact or approximate *trans* couples of a coordination sphere.

Obtaining the LF parameters enables a deeper insight into the magnetism of the presented compounds. Consequently, we employed an approximation known as the Steven's equivalent operators.[50,51] This gives the LF split of the ground multiplets J of lanthanides needing only the LF parameters (*i.e.* the values from Tables S1 or S2, from the ESI†), without demanding the explicit spin–orbit or the inter-electronic (Slater–Condon) integrals. This method consists of using triads of coefficients specific to each lanthanide and its J ground state, multiplying respectively the LF parameters of the second, fourth and sixth ranks. The procedure retrieves relatively well the *ab initio* computed LF-SO levels, being trustful for the analysis depicted in the Fig. 7. In this way, we can find conveniently the composition of each state from the LF driven J spectrum, in terms of J_z projections. The histograms drawn at each level correspond to the relative percentage of the
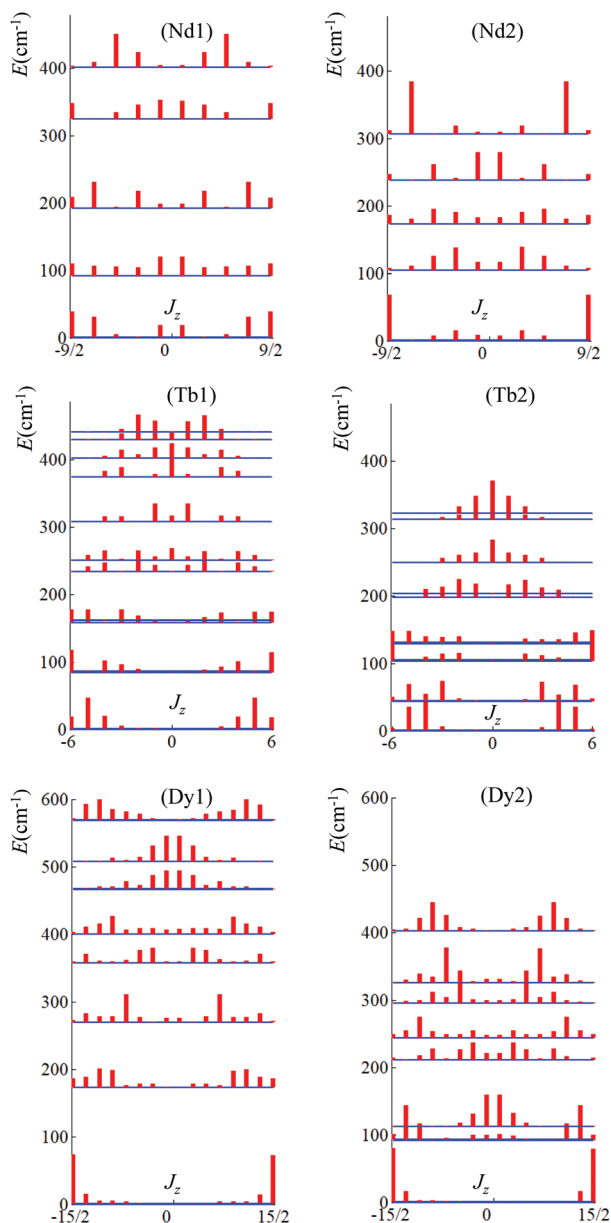
Fig. 7 The ligand field split of the J of the ground J of the Ln^{3+} ions. The left side corresponds to site 1, while the right side stands for site 2. The vertical bars at each levels mark, in relative scaling the percentage of J_z projections contributing to the given state.

With the non-routine post-computational treatment of the CASSCF-SO data, we emulated the *ab initio* magnetic susceptibility. The anisotropic magnetic susceptibility for a direction given by the $\{\theta, \varphi\}$ couple of polar coordinates is expressed as:

$$\chi(\theta,\varphi) = \left(\frac{d^2}{dB^2}\ln(Z(\theta,\varphi,B))\right)_{\theta,\varphi}$$

where Z is the sum function:

$$Z(\theta,\varphi,B) = \sum_i \mathrm{Exp}(-E_i(\theta,\varphi,B)/k_\mathrm{B}T).$$

The averaged susceptibility corresponds to the average on the orientations:

$$\bar{\chi} = (1/4\pi)\int_{\theta=0}^{\theta=\pi}\int_{\varphi=0}^{\varphi=2\pi}\chi(\theta,\varphi)\sin(\theta)\mathrm{d}\theta\mathrm{d}\varphi$$

The derivatives were estimated numerically, with a $dB = 0.01$ T finite difference, while the integration was approximated as sum over a 24 × 48 mesh of the θ, φ variables. Summing the simulated the T *vs.* $\chi_\mathrm{M}T$ curves of the two sites, one obtains patterns similar to the experimental curves, as illustrated in the bottom panel of Fig. 4. The small quantitative deviations are totally acceptable in light of inherent approximations present even at the *ab initio* level of computer experiments.

The magnetic susceptibility on the directions of the Cartesian frame, after setting the z line along the easy axes of ground states, is given in S16–S21.† Because the ground level carries the maximal moment of the given multiplet under the ligand field in all the cases, the $\chi_\mathrm{M}T$ *vs.* T curve along the z axis has a descendent pattern. With the onset of thermal averaging, the levels with a lower magnetic response are populated. Conversely, the $\chi_\mathrm{M}T$ dependencies along the x and y lines start from lower values, increase with T, since the states with magnetic responses along these directions are placed on a higher position in the LF spectrum of the J multiplet. On average, the increasing pattern dominates.

We tested through calculations that the $[W(CN)_8]^{4-}$ ion is magnetically silent. This is due to the contribution of the large ligand field with a strong spin–orbit coupling. With appropriate modelling experiments, it was probed that the magnetic response of the $[W(CN)_8]^{4-}$ compounds is very sensitive to the coordination geometry. Thus, in an antiprism elongated geometry along the fourfold axis, the ground state carries a magnetic moment close to the ideal estimation for the maximal projection from a $^3F_2$ term. In a compressed antiprism geometry, the ground state is non-magnetic, the effective moment being carried in excited components. When a distortion from a fourfold symmetry is present, *e.g.* moving from D_{4d} to D_{2d} by transforming the square faces to diamonds, all the states from the ^3F origin become almost magnetically silent. Therefore, the observed magnetism of the compounds studied is effectively due to the lanthanide ions.

An analysis of the exchange coupling between lanthanide ions was performed for the gadolinium compounds. Dimeric

J_z elements in the corresponding wavefunction. The diagrams are symmetric with respect to the $\pm J_z$ couples. One may observe that the ground states are made preponderantly of elements close to the extremal projections, $J_z = \pm J$. Such a situation is well evidenced for the Dy case, where, for both sites, the ground state consists of almost pure $\pm 15/2$ components. For the other states of each spectrum, there is no simple formula to understand the pattern. One may find however that the states with low amplitude in the lobes of computed magnetization polar maps have compositions made of null or small J_z projections.

This journal is © the Partner Organisations 2018

Inorg. Chem. Front., 2018, **5**, 1967–1977 | **1973**

units were cut from the experimental structure corresponding to the Gd1–Gd1 and Gd2–Gd2 pairs, discarding the Gd1–Gd2 part of the chain, because of the obvious large separation between ions. With CASSCF(14,14) calculations in both molecular models we obtained weak ferromagnetic coupling, with a very small value for the first case, $J_{Gd1–Gd1} = 1.3 \times 10^{-5}$ cm^{-1} and a small one for the site 2 correspondent, $J_{Gd2–Gd2} = 9.5 \times 10^{-3}$ cm^{-1}. To verify these outcomes, we performed Broken-Symmetry (BS) DFT calculations[61] on the same systems obtaining about $J = 0.01$ cm^{-1} for both types of symmetric dimeric moieties. The situation may be corroborated with the experimental findings suggesting either weak ferromagnetism or uncoupled limits. There is a good match between CASSCF *vs.* DFT estimation for site 2. In the other case, possibly the BS-DFT is less precise, detecting in the final spin maps a leakage of spin density on the bridges, larger than expected for the confined f electrons. In spite of small values, one may accept that the coupling is, indeed, ferromagnetic.

The inter-centre coupling has a small impact on the magnetic properties, being active only at a very low temperature. To complete the analysis, we aimed at the *ab initio* estimation of the Zero Field Splitting parameters, performing CASSCF-SO calculations at each gadolinium site, replacing the above-mentioned dimers with diamagnetic lutetium. The spin–orbit spectrum included the levels related to the ^{8}S atomic ground term and all the sextets of the f^7 configuration: ^{6}P, ^{6}D, ^{6}F, ^{6}G, ^{6}H and ^{6}I. The lowest eight eigenvalues present in doublets correspond to the ZFS spectrum. Their doublet nature is due to the fact that the phenomenological ZFS Hamiltonian of Gd^{3+}, *i.e.* a matrix of 8 × 8 size, is factorized in two equivalent 4 × 4 blocks:[52]

$$\det \begin{pmatrix} 7D - x & \sqrt{21}E & 0 & 0 \\ \sqrt{21}E & -3D - x & 2\sqrt{15}E & 0 \\ 0 & 2\sqrt{15}E & -5D - x & 3\sqrt{5}E \\ 0 & 0 & 3\sqrt{5}E & D - x \end{pmatrix} = 0.$$

The computed ZFS spectra match well with the following effective parameters: $D_1 = 0.0285$ cm^{-1} and $E_1 = 0.0155$ cm^{-1} for site 1, while $D_2 = 0.0613$ and $E_2 = 0.0245$ for site 2. Introduced in the simulation of $\chi_M T$ curves, the above values exhibit trends resembling the antiferromagnetic pattern. This prompts us to regard the experimental situation as a competition between the weak ferromagnetism of the Gd–Gd couplings and the local small anisotropy of the Gd sites. We point that, although getting small absolute values for the ZFS parameters and the exchange coupling, the *ab initio* calculations are relatively reliable in a qualitative sense. These calculations may have errors amounting to a certain fraction from the expected range of a given quantity, while are safe in the reproduction of the mechanism, trends and relative values.[53]

When the magnetism of the Gd-based chain is approximated as a dimer and the ZFS values for site 1 are imposed, one obtains a pattern with a shallow maximum at low temperatures and a value around $J_{Gd–Gd} = 0.02$ cm^{-1} for the exchange. This looks alike to antiferro in the left domain, and like ferro on the right side, before reaching the paramagnetic plateau.

One may propose that this is qualitatively similar to the low-temperature details of compound 2 (see Fig. 4). For the ZFS parameters of site 2, a similar trend is reached at about $J_{Gd–Gd}$ 0.04 cm^{-1}. Then, assuming that the *ab initio* estimation of ZFS parameters is more stable than those of the exchange, one may obtain in this way a range of ferromagnetic coupling. Even the apparent paramagnetism of compound **6** can be supposed as a *null-game* between the trends given by the ZFS and exchange part, considering the compounds as having a weak but yet sizeable ferromagnetism.

Conclusions

A new series of isostructural lanthanide-based cyanide-bridged assemblies were obtained by self-assembling Ln^{3+} ions (Ln^{3+} = Nd, Gd, Tb and Dy) and [M(CN)$_8$]$^{4-}$ (M^{4+} = Mo and W) building-blocks in the presence of pyrazine-2,3-dicarboxylate acid. The obtained 3D dense networks have 1D open channels which are occupied by K$^+$ ions and water molecules. Detailed experimental and theoretical studies show that the magnetic interaction between the Gd^{3+} ions is weakly ferromagnetic for the compound containing [Mo(CN)$_8$]$^{4-}$ units whilst the Gd^{3+} ions are not coupled in the analogue compound obtained from the [W(CN)$_8$]$^{4-}$ building-blocks. At the same time, the magnetic properties of Nd^{3+}, Tb^{3+}, and Dy^{3+} compounds are dominated by the interplay between the ligand field and spin–orbit effects, with a little impact from the magnetic super-exchange interaction between the lanthanide ions. The theoretical calculations confirm indeed that the recorded magnetism of the presented systems is mainly due to the strong magnetic anisotropy of the lanthanide ions. We foresee that further research on these types of materials will emerge in the direction of advanced multifunctional materials.

Experimental

Materials

Lanthanide nitrates, pyrazine-2,3-dicarboxylic acid, and all the solvents were commercially available (Aldrich, >99% pure) and used as received. The K$_4$[M(CN)$_8$]·2H$_2$O (M^{4+} = Mo and W) precursors were synthesized as reported previously.[24]

Synthesis

A solution of Ln(NO$_3$)$_3$·5H$_2$O (Ln = Nd, Gd, Tb, and Dy) (1 mmol, 440 mg) in water (5 mL) was added to a suspension of pyrazine-2,3-dicarboxylic acid (1 mmol, 173 mg) in water (5 mL). The reaction mixture was stirred for 5 min at room temperature until it became a clear solution. Then, this mixture was added to a solution of K$_4$[M(CN)$_8$]·4H$_2$O (1 mmol, 530 mg (Mo) and 620 mg (W)) in water (2 ml). The slow diffusion of methanol into the water mixture (1 : 2 volume ratio) gave crystalline orange materials within 2 days.

{KH[Nd$_2$(pzdc)$_2$(CH$_3$OH)(H$_2$O)$_7$][Mo(CN)$_8$]}·5H$_2$O (1). Yield: 628 mg (57%). C, H, N analysis (%): calcd C 20.34, H 2.46,

1974 | *Inorg. Chem. Front.*, 2018, **5**, 1967–1977

This journal is © the Partner Organisations 2018

N 14.24; found C 20.42, H 2.11, N 14.63. FTIR (KBr, cm^{-1}): 3427 br, 2117 s, 1622 m, 1568 m, 1448 w, 1442 m, 1379 m, 1243 m, 1216 m, 1121 s, 1075 m, 901 w, 852 w.

{KH[Gd$_2$(pzdc)$_2$(CH$_3$OH)(H$_2$O)$_7$][Mo(CN)$_8$]}·5H$_2$O (2). Yield: 464 mg (42%). C, H, N analysis (%): calcd C 19.29, H 2.65, N 13.5; found C 19.41, H 2.66, N 11.08. FTIR (KBr, cm^{-1}): 3353 br, 2129 s, 2097 m, 1611 m, 1566 m, 1445 w, 1396 m, 1362 m, 1206 m, 1169 m, 1119 s, 1074 m, 896 w, 843 w.

{KH[Tb$_2$(pzdc)$_2$(CH$_3$OH)(H$_2$O)$_7$][Mo(CN)$_8$]}·5H$_2$O (3). Yield: 680 mg (62%). C, H, N analysis: (%) calcd C 21.75, H 2, N 14.50; found C 20.16, H 3.45, N 13.23. FTIR (KBr, cm^{-1}): 3360 br, 2127 s, 2010 m, 1610 m, 1568 m, 1445 w, 1395 m, 1363 m, 1207 m, 1170 m, 1120 s, 1075 m, 896 w, 845 w.

{KH[Dy$_2$(pzdc)$_2$(CH$_3$OH)(H$_2$O)$_7$][Mo(CN)$_8$]}·5H$_2$O (4). Yield: 700 mg (65%). C, H, N analysis (%): calcd C 21.89 H 2.01, N 14.59; found C 19.33, H 3.54, N 13.8. FTIR (KBr, cm^{-1}): 3354 br, 2130 s, 2096 m, 1611 m, 1567 m, 1446 w, 1396 m, 1360 m, 1206 m, 1170 m, 118 s, 1072 m, 896 w, 846 w.

{KH[Nd$_2$(pzdc)$_2$(CH$_3$OH)(H$_2$O)$_7$][W(CN)$_8$]}·5H$_2$O (5). Yield: 737 mg (62%). C, H, N analysis: (%) calcd C 18.40, H 2.53, N 12.88; found C 18.44, H 1.78, N 14.47. FTIR (KBr, cm^{-1}): 3535 br, 2119 s, 2097 m, 1615 m, 1567 m, 1451 w, 1418 m, 1376 m, 1245 m, 1215 m, 1124 s, 1077 m, 903 w, 852 w.

{KH[Gd$_2$(pzdc)$_2$(CH$_3$OH)(H$_2$O)$_7$][W(CN)$_8$]}·5H$_2$O (6). Yield: 692 mg (58%). C, H, N analysis (%): calcd C 18.02, H 2.48, N 12.61; found C 18.3, H 1.70, N 14.51. FTIR (KBr, cm^{-1}): 3416 br, 2115 s, 2096 m, 1617 m, 1573 m, 1451 w, 1424 m, 1377 m, 1248 m, 1221 m, 1125 s, 1075 m, 903 w, 858 w.

{KH[Tb$_2$(pzdc)$_2$(CH$_3$OH)(H$_2$O)$_7$][W(CN)$_8$]}·5H$_2$O (7). Yield: 740 mg (66%). C, H, N analysis (%): calcd C 20.34, H 1.87, N 13.55; found C 18.8, H 3.48, N 12.51. FTIR (KBr, cm^{-1}): 3415 br, 2117 s, 2096 m, 1620 m, 1570 m, 1450 w, 1424 m, 1379 m, 1248 m, 1220 m, 1129 s, 1075 m, 900 w, 856 w.

{KH[Dy$_2$(pzdc)$_2$(CH$_3$OH)(H$_2$O)$_7$][W(CN)$_8$]}·5H$_2$O (8). Yield: 760 mg (68%). C, H, N analysis (%): calcd C 20.22, H 1.86, N 13.47; found C 19.48, H 3.06, N 13.12. FTIR (KBr, cm^{-1}): 3410 br, 2120 s, 2096 m, 1620 m, 1577 m, 1451 w, 1422 m, 1377 m, 1248 m, 1219 m, 1125 s, 1075 m, 906 w, 860 w.

Physical measurements

Infrared spectra (4000–400 cm^{-1}, resol. 0.5 cm^{-1}) were recorded using a Varian 660 FTIR spectrometer using KBr pellets and the transmission technique. Powder X-ray diffraction (PXRD) was carried out on a Rigaku Miniflex X-ray Diffractometer. Measurements were performed from 3° to 50° with a turning speed of 2.0° min^{-1}. Thermogravimetric analysis (TGA) and differential scanning calorimetry (DSC) were performed using a NETZSCH Jupiter® STA 449F3 instrument. The measurements were carried under argon (20 ml min^{-1}) at 35–900 °C. Diffuse reflectance spectra were obtained on a Perkin–Elmer Lambda 900 spectrophotometer using MgO as a reference.

X-ray single-crystal structure determination

The single-crystal structure of compound 5 was determined based on the crystallographic data collected using a beamline 11.3.1 at the Advanced Light Source, Lawrence Berkeley National Lab. Samples were mounted on MiTeGen kapton loops and placed on the goniometer head of a Bruker D8 diffractometer equipped with a PHOTON100 CMOS detector operating in shutterless mode. The samples were in a 100 K nitrogen cold stream provided by an Oxford Cryostream 800 Plus low temperature apparatus. Diffraction data were collected using synchrotron radiation monochromated by using silicon (111) to a wavelength of 0.7749 (1) Å. The structure was solved by intrinsic phasing (SHELXT) and refined by fullmatrix least-squares on F^2 (SHELXL-2014). Crystallographic data are registered at the Cambridge Structural Data Base as CCDC 1818714.†

Magnetic measurements

Variable-temperature (2.0–10 K) alternating current (ac) magnetic susceptibility measurements under ±5.0 G oscillating field at frequencies in the range of 0.1–10 kHz were carried out on crystalline samples under 0 and 1 kG applied static dc fields with a Quantum Design Physical Property Measurement System (PPMS).

Calculations and modelling

Ab initio[54,55] calculations were performed with GAMESS code,[56] using fragment geometries cut from the experimental crystal structure.[31] The lanthanide center was accounted for by the effective core potential basis set of SBKJC type (Stevens–Basch–Krauss–Jasien–Cundari).[57–59] The tungsten atom was accounted for by the SARC-ZORA basis set[60] The O and N atoms were treated with the 6-311G* basis, while the C and H atoms remaining in the ligand structure were treated with the 6-31G basis. The magnetic properties were discussed with subsequent modelling based on the data extracted from the black box of Complete Active Space Self Consistent Field (CASSCF) calculations complemented with Spin–Orbit (SO) treatment. To asses exchange coupling parameters we also used Broken Symmetry (BS),[61] in the frame of Density Functional Theory[62] (DFT) realized with the B3LYP option. We retrieved the orbital components of the Zeeman Hamiltonian by extracting extra-output from the black box of the computation, namely the matrix elements of the L_x, L_y and L_z operators. This part as well as the spin-type Zeeman part enabled the explicit implementation of the magnetic field dependence in the CASSCF-SO matrix.

Conflicts of interest

There are no conflicts to declare.

Acknowledgements

This journal is © the Partner Organisations 2018

Inorg. Chem. Front., 2018, **5**, 1967–1977 | **1975**

References

1 M. T. Gamer, Y. Lan, P. W. Roesky, A. K. Powell and R. Clérac, *Inorg. Chem.*, 2008, **47**, 6581–6583.

2 D. Gatteschi, O. Kahn, J. S. Miller and F. Palacio, *Magnetic molecular materials*, Springer Science & Business Media, 2012.

3 Y. S. Ding, N. F. Chilton, R. E. Winpenny and Y. Z. Zheng, *Angew. Chem., Int. Ed.*, 2016, **128**, 16305–16308.

4 B. Sieklucka and D. Pinkowicz, *Molecular magnetic materials: concepts and applications*, John Wiley & Sons, 2017.

5 H.-L. Sun, Z.-M. Wang and S. Gao, *Coord. Chem. Rev.*, 2010, **254**, 1081–1100.

6 S. Demir, I.-R. Jeon, J. R. Long and T. D. Harris, *Coord. Chem. Rev.*, 2015, **289**, 149–176.

7 Y.-S. Meng, S.-D. Jiang, B.-W. Wang and S. Gao, *Acc. Chem. Res.*, 2016, **49**, 2381–2389.

8 S. Haas, E. Heintze, S. Zapf, B. Gorshunov, M. Dressel and L. Bogani, *Phys. Rev. B: Condens. Matter Mater. Phys.*, 2014, **89**, 174409.

9 K. Liu, H. Li, X. Zhang, W. Shi and P. Cheng, *Inorg. Chem.*, 2015, **54**, 10224–10231.

10 K. S. Pedersen, A. Vindigni, R. Sessoli, C. Coulon and R. Clérac, *Single-Chain Magnet, in Molecular Magnetic Materials: Concepts and Applications*, 2016, pp. 131–159.

11 S. G. McAdams, A.-M. Ariciu, A. K. Kostopoulos, J. P. Walsh and F. Tuna, *Coord. Chem. Rev.*, 2017, **346**, 216–239.

12 S. K. Gupta and R. Murugavel, *Chem. Commun.*, 2018, **54**, 3685–3696.

13 G. Lorusso, J. W. Sharples, E. Palacios, O. Roubeau, E. K. Brechin, R. Sessoli, A. Rossin, F. Tuna, E. J. McInnes and D. Collison, *Adv. Mater.*, 2013, **25**, 4653–4656.

14 S. Biswas, H. S. Jena, A. Adhikary and S. Konar, *Inorg. Chem.*, 2014, **53**, 3926–3928.

15 F. Troiani and M. Affronte, *Chem. Soc. Rev.*, 2011, **40**, 3119–3129.

16 V. Garcia and M. Bibes, *Nat. Commun.*, 2014, **5**, 4289.

17 N. Bridonneau, L. M. Chamoreau, P. P. Laine, W. Wernsdorfer and V. Marvaud, *Chem. Commun.*, 2013, **49**, 9476–9478.

18 K. R. Vignesh, S. K. Langley, K. S. Murray and G. Rajaraman, *Chem. – Eur. J.*, 2017, **23**, 1654–1666.

19 P. Z. Moghadam, A. Li, S. B. Wiggin, A. Tao, A. G. P. Maloney, P. A. Wood, S. C. Ward and D. Fairen-Jimenez, *Chem. Mater.*, 2017, **29**, 2618–2625.

20 S. Mohapatra, B. Rajeswaran, A. Chakraborty, A. Sundaresan and T. K. Maji, *Chem. Mater.*, 2013, **25**, 1673–1679.

21 K. Liu, X. Zhang, X. Meng, W. Shi, P. Cheng and A. K. Powell, *Chem. Soc. Rev.*, 2016, **45**, 2423–2439.

22 P. H. Lin, T. J. Burchell, R. Clérac and M. Murugesu, *Angew. Chem., Int. Ed.*, 2008, **120**, 8980–8983.

23 L. Ungur, S.-Y. Lin, J. Tang and L. F. Chibotaru, *Chem. Soc. Rev.*, 2014, **43**, 6894–6905.

24 P. Zhang, Y.-N. Guo and J. Tang, *Coord. Chem. Rev.*, 2013, **257**, 1728–1763.

25 R. Sessoli and A. K. Powell, *Coord. Chem. Rev.*, 2009, **253**, 2328–2341.

26 M. Andruh, J.-P. Costes, C. Diaz and S. Gao, *Inorg. Chem.*, 2009, **48**, 3342–3359.

27 F. Prins, E. Pasca, L. J. de Jongh, H. Kooijman, A. L. Spek and S. Tanase, *Angew. Chem., Int. Ed.*, 2007, **46**, 6081–6084.

28 S. Chorazy, M. Rams, M. Wyczesany, K. Nakabayashi, S.-I. Ohkoshi and B. Sieklucka, *CrystEngComm*, 2018, **20**, 1271–1281.

29 B. Nowicka, T. Korzeniak, O. Stefańczyk, D. Pinkowicz, S. Chorąży, R. Podgajny and B. Sieklucka, *Coord. Chem. Rev.*, 2012, **256**, 1946–1971.

30 S. Chorazy, K. Nakabayashi, S.-I. Ohkoshi and B. Sieklucka, *Chem. Mater.*, 2014, **26**, 4072–4075.

31 S. Tanase, M. Ferbinteanu and F. Cimpoesu, *Inorg. Chem.*, 2011, **50**, 9678–9687.

32 S. Tanase, M. C. Mittelmeijer-Hazeleger, G. Rothenberg, C. Mathonière, V. Jubera, J. M. M. Smits and R. de Gelder, *J. Mater. Chem.*, 2011, **21**, 15544.

33 Z. X. Wang, X. F. Shen, J. Wang, P. Zhang, Y. Z. Li, E. N. Nfor, Y. Song, S. Ohkoshi, K. Hashimoto and X. Z. You, *Angew. Chem., Int. Ed.*, 2006, **45**, 3287–3291.

34 S. Chorazy, M. Rams, K. Nakabayashi, B. Sieklucka and S. I. Ohkoshi, *Chem. – Eur. J.*, 2016, **22**, 7371–7375.

35 H. Zhou, Q. Chen, A.-H. Yuan, H.-B. Zhou, X.-P. Shen, L. Chen and Y. Song, *Cryst. Growth Des.*, 2017, **17**, 6523–6530.

36 H. Yin and S.-X. Liu, *Polyhedron*, 2007, **26**, 3103–3111.

37 L.-P. J. Xiang-Jun Zheng and Shao-Zhe Lu, *Eur. J. Inorg. Chem.*, 2002, 3356.

38 X.-Y. Hou, X. Wang, L. J. Gao, F. Fu, J. J. Wang and J. Cao, *Z. Anorg. Allg. Chem.*, 2014, **640**, 2072–2077.

39 S. A. Bhat, M. Faizan, M. J. Alam and S. Ahmad, *Spectrosc. Lett.*, 2016, **49**, 449–457.

40 W. Wu, A. M. Kirillov, X. Yan, P. Zhou, W. Liu and Y. Tang, *Angew. Chem., Int. Ed.*, 2014, **53**, 10649–10653.

41 S. Decurtins, M. Gross, H. W. Schmalle and S. Ferlay, *Inorg. Chem.*, 1998, **37**, 2443–2449.

42 O. Kahn, *Molecular Magnetism*, VCH Publishers, Inc., USA, 1993, 1993, 393.

43 M. Andruh, E. Bakalbassis, O. Kahn, J. C. Trombe and P. Porcher, *Inorg. Chem.*, 1993, **32**, 1616–1622.

44 R. Carlin, *Magnetochemistry*, Wiley, New York, 1980.

45 D. N. Woodruff, R. E. Winpenny and R. A. Layfield, *Chem. Rev.*, 2013, **113**, 5110–5148.

1976 | *Inorg. Chem. Front.*, 2018, **5**, 1967–1977

This journal is © the Partner Organisations 2018

46 A. Pascual-Álvarez, J. Vallejo, E. Pardo, M. Julve, F. Lloret, J. Krzystek, D. Armentano, W. Wernsdorfer and J. Cano, *Chem. – Eur. J.*, 2015, **21**, 17299–17307.

47 F. Luis, J. Bartolomé, J. Fernández, J. Tejada, J. Hernández, X. Zhang and R. Ziolo, *Phys. Rev. B: Condens. Matter Mater. Phys.*, 1997, **55**, 11448.

48 M. Ferbinteanu, F. Cimpoesu and S. Tanase, in *Lanthanide Metal-Organic Frameworks*, Springer, 2014, pp. 185–229.

49 C. Schaffer, *Theor. Chim. Acta*, 1966, **4**, 166.

50 K. W. H. Stevens, *Proc. Phys. Soc., London, Sect. A*, 1952, **65**, 209–215.

51 H. Lueken, *Magnetochemie*, B. G. Teubner, Stuttgart, Leipzig, 1999.

52 M. Ferbinteanu, F. Cimpoesu, M. A. Gîrtu, C. Enachescu and S. Tanase, *Inorg. Chem.*, 2012, **51**, 40–50.

53 M. V. Putz, F. Cimpoesu and M. Ferbinteanu, *Structural Chemistry. Principles, Methods, and Case Studies*, Springer, 2018.

54 F. Jensen, *Introduction to computational chemistry*, John Wiley & Sons, 2017.

55 B. O. Roos, *Advances in Chemical Physics: Ab Initio Methods in Quantum Chemistry Part 2*, 2007, vol. 69, pp. 399–445.

56 M. Schmidt, K. Baldridge, J. Boatz, S. Elbert, M. Gordon, J. Jensen, S. Koseki, N. Matsunaga, K. Nguyen and S. Su, *J. Comput. Chem.*, 1993, **14**, 1347–1363.

57 T. R. Cundari and W. J. Stevens, *J. Chem. Phys.*, 1993, **98**, 5555–5565.

58 W. J. Stevens, H. Basch and M. Krauss, *J. Chem. Phys.*, 1984, **81**, 6026–6033.

59 W. J. Stevens, M. Krauss, H. Basch and P. G. Jasien, *Can. J. Chem.*, 1992, **70**, 612–630.

60 D. A. Pantazis, X.-Y. Chen, C. R. Landis and F. Neese, *J. Chem. Theory Comput.*, 2008, **4**, 908–919.

61 L. Noodleman, *J. Chem. Phys.*, 1981, **74**, 5737–5743.

62 W. Koch and M. C. Holthausen, *A chemist's guide to density functional theory*, John Wiley & Sons, 2015.